



MgH₂ dehydrogenation properties improved by MnFe₂O₄ nanoparticles



Ping Li^{a,*}, Qi Wan^a, Ziliang Li^a, Fuqiang Zhai^a, Yunlong Li^a, Liquan Cui^a,
Xuanhui Qu^{a,b}, Alex A. Volinsky^c

^a Institute for Advanced Materials and Technology, University of Science and Technology Beijing, Beijing 100083, China

^b State Key Laboratory for Advanced Metals and Materials, University of Science and Technology Beijing, Beijing 100083, China

^c Department of Mechanical Engineering, University of South Florida, Tampa, FL 33620, USA

HIGHLIGHTS

- MnFe₂O₄ nanoparticles effect on MgH₂ desorption properties is studied for the first time.
- MgH₂ + 7 mol% MnFe₂O₄ desorption temperature onset reduction is 140 °C, compared with MgH₂.
- The apparent activation energy of the 7 mol% MnFe₂O₄-doped sample is dramatically decreased.
- Mg₂MnO₄ and Fe_{0.872}O phases play an important role in improving MgH₂ desorption properties.

ARTICLE INFO

Article history:

Received 5 December 2012

Received in revised form

2 March 2013

Accepted 7 March 2013

Available online 26 March 2013

Keywords:

Manganese ferrite

Hydrogen storage

Magnesium hydride

Dehydrogenation temperature

Apparent activation energy

ABSTRACT

The catalytic effects of MnFe₂O₄ nanoparticles on the dehydrogenation properties of MgH₂, prepared by ball milling, are investigated for the first time. The onset dehydrogenation temperature for MgH₂ + 7 mol % MnFe₂O₄ is 300 °C, 140 °C lower, compared with the as-received MgH₂. The isothermal dehydriding kinetics shows that 7 mol% MnFe₂O₄-doped sample can release 5.05 wt.% hydrogen in 1 h at 300 °C under 0.1 MPa pressure, whereas as-received MgH₂ releases only 0.49 wt.% hydrogen for the same conditions, indicating significantly improved dehydrogenation. From the differential scanning calorimetry and the Kissinger desorption kinetics analysis, the apparent activation energy of 7 mol% MnFe₂O₄-doped sample is 64.55 kJ mol^{−1}, resulting in 190.34 kJ mol^{−1} decrease, compared with the as-received MgH₂, which is lower than that of MgH₂ doped with other reported transition metal oxide catalysts. Based on X-ray diffraction and X-ray photoelectron spectroscopy tests, Mg₂MnO₄ and Fe_{0.872}O phases together play a synergistic role in remarkably improving MgH₂ dehydriding properties.

© 2013 Elsevier B.V. All rights reserved.

1. Introduction

Magnesium hydride is one of the attractive hydrogen storage materials due to its high hydrogen storage capacity (~7.6 wt.%), low cost and light weight. However, high desorption temperature (>400 °C) and relatively poor hydriding–dehydriding kinetics limit MgH₂ practical applications [1–5]. During the past decade researchers tried to address these issues. The efforts included preparing smaller particle powders by using ball milling [6], and additives, such as transition metals [4,7], transition oxides [8,9], transition halides [10], and other compounds [5,11]. Since transition metals have multiple valence states in corresponding transition metal oxides, the latter show better reaction efficiency [9,12]. Thus,

studying hydrogen interactions with transition metal oxides helps understanding their specific role in MgH₂ hydrogen absorption–desorption reactions [13–16]. It was also reported that MnO₂ and Fe₂O₃ could ameliorate MgH₂ hydrogen storage performance [17,18]. Zhai et al. reported that MnFe₂O₄ could remarkably improve LiAlH₄ dehydrogenation [19], therefore, it is reasonable to believed that MnFe₂O₄ would show great potential as a catalyst to advance MgH₂ hydrogen storage performance. In this work, MnFe₂O₄ nanoparticles were employed as catalyst precursors to study their effect on the dehydrogenation properties of MgH₂ prepared by ball milling.

2. Experimental

MgH₂ was obtained from Sigma Aldrich Co., and MnFe₂O₄ (≥99.99% pure, 20 nm particle size) was prepared by the nitrate–

* Corresponding author.

E-mail address: ustbliping@126.com (P. Li).

citrate auto-combustion methods ($\text{Fe}(\text{NO}_3)_3 \cdot 9\text{H}_2\text{O}$ and $\text{Mn}(\text{NO}_3)_2$ were dissolved in deionized water and mixed uniformly, then adding chelating agent citric acid, the pH value of solution was adjusted to 7 by adding $\text{NH}_3 \cdot \text{H}_2\text{O}$, the solution was stirred by magnetic stirrer at 60°C to form a sol–gel, the gel was dried at 120°C . The dry gel was ignited in the air and a self-propagation reaction (exothermic) followed. Both materials were used as-received, without any further purification. All handling (including weighing and loading) was performed in high-purity argon-filled glove box in order to avoid oxidation and moisture. About 2 g of MgH_2 was mixed in different proportions (3 mol%, 5 mol%, 7 mol%, and 9 mol%) with MnFe_2O_4 nanoparticles, and ball milled for 30 min in a high-energy Spex mill. All the samples were loaded into the stainless steel vial in an argon-filled glove box. ZrO_2 balls were added with a ball-to-powder weight ratio of 15:1. After the 10 min ball milling, the steel vial was rested for 5 min to cool it.

The dehydrogenation properties of as-received MgH_2 and doped samples were measured by using a pressure–composition–temperature (PCT) apparatus (Beijing Nonferrous Metal Research Institute, China). For non-isothermal dehydrogenation, typically, 0.5 g sample was loaded into the vessel, and then heated up to 500°C at a 6°C min^{-1} rate under 0.1 atm, the system pumped to a hard vacuum, before heating was commenced. Following the first complete dehydrogenation, the samples were subjected to rehydrogenation at 350°C under 4 MPa hydrogen pressure. Subsequently, the rehydrogenated samples were dehydrogenated at 300°C , or 350°C under 0.1 MPa pressure, respectively.

In order to further analyze the dehydrogenation performance and calculate the desorption activation energy of the doped MgH_2 sample by means of the Kissinger method, the differential scanning calorimetry (DSC) was performed using NETZSCH STA 449C in high-purity argon (50 mL min^{-1} flow rate). About 5 mg sample was sealed into a 50 mL alumina crucible in the glove box, and then heated at different heating rates (4°C min^{-1} , 7°C min^{-1} and $10^\circ\text{C min}^{-1}$), from 50°C to 500°C .

The morphology of the as-received and doped samples after ball milling was examined by scanning electron microscopy (SEM, ZEISS EVO18, Germany). The phase structure of the samples after ball milling and after dehydrogenation was determined by using the MXP21VAHF X-ray diffractometer (XRD with $\text{Cu K}\alpha$ radiation, 40 kV, 200 mA) at room temperature. The 2θ angle was varied from 10° to 90° in 0.02° increments, 1 s per step. X-ray photoelectron spectroscopy (XPS) was performed with the PHI-5300 spectrometer.

3. Results and discussion

3.1. Dehydrogenation temperature

Fig. 1 shows the non-isothermal desorption curves of as-received MgH_2 , as-milled MgH_2 , and MgH_2 doped with 3 mol%, 5 mol%, 7 mol% and 9 mol% MnFe_2O_4 nanopowder. It is distinct that adding MnFe_2O_4 nanoparticles dramatically improves MgH_2 dehydriding properties, since the onset desorption temperature for the doped samples is remarkably lower, compared with the as-received MgH_2 . The as-received MgH_2 starts to decompose at 440°C . Compared with the as-received MgH_2 , the initial dehydrogenation temperature of the as-milled MgH_2 drops by 80°C due to the MgH_2 activation introduced by the ball milling [20,21].

When MgH_2 matrix is doped with MnFe_2O_4 nanoparticles, the desorption temperature onset is reduced further. For the 3 mol% doped sample, the dehydrogenation process initiates at 330°C . Further increase of the additives amount to 5 mol% reduces the dehydrogenation temperatures to 320°C . Compared with the as-received MgH_2 , adding 3 mol% and 5 mol% MnFe_2O_4 causes a

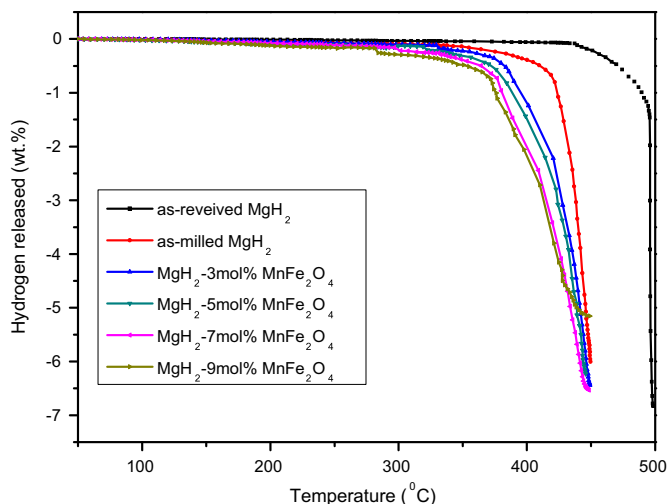


Fig. 1. Thermal desorption curves of the as-received MgH_2 , as-milled MgH_2 , and ball-milled MgH_2 doped with 3 mol%, 5 mol%, 7 mol% and 9 mol% nanosized MnFe_2O_4 .

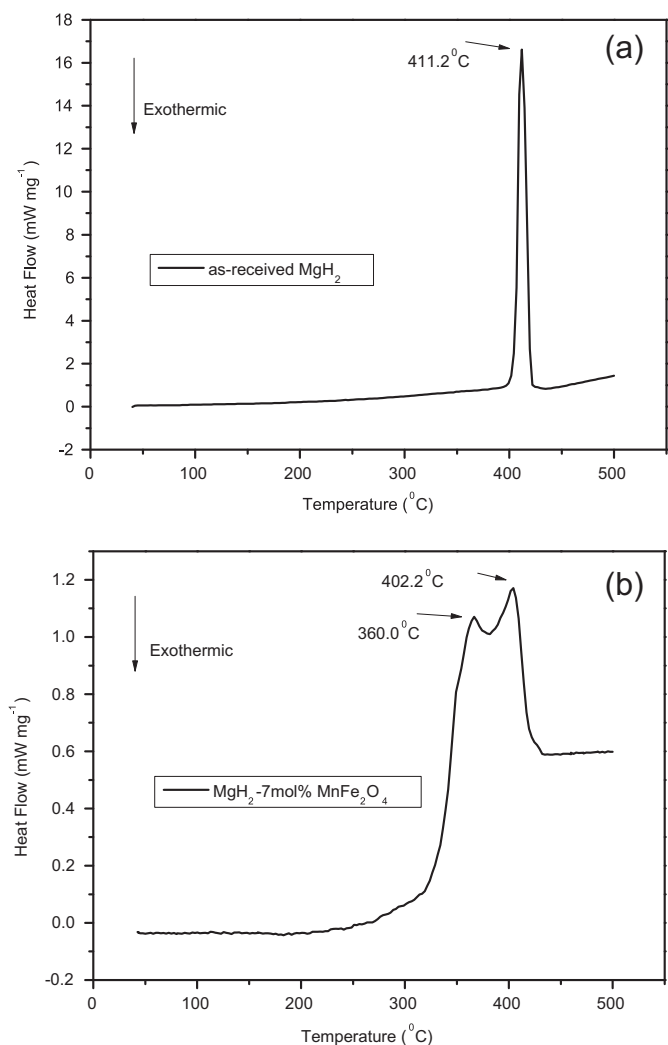


Fig. 2. DSC profiles of (a) as-received MgH_2 and (b) ball-milled MgH_2 doped with 7 mol% MnFe_2O_4 within the 50 – 500°C temperature range (4°C min^{-1} heating rate).

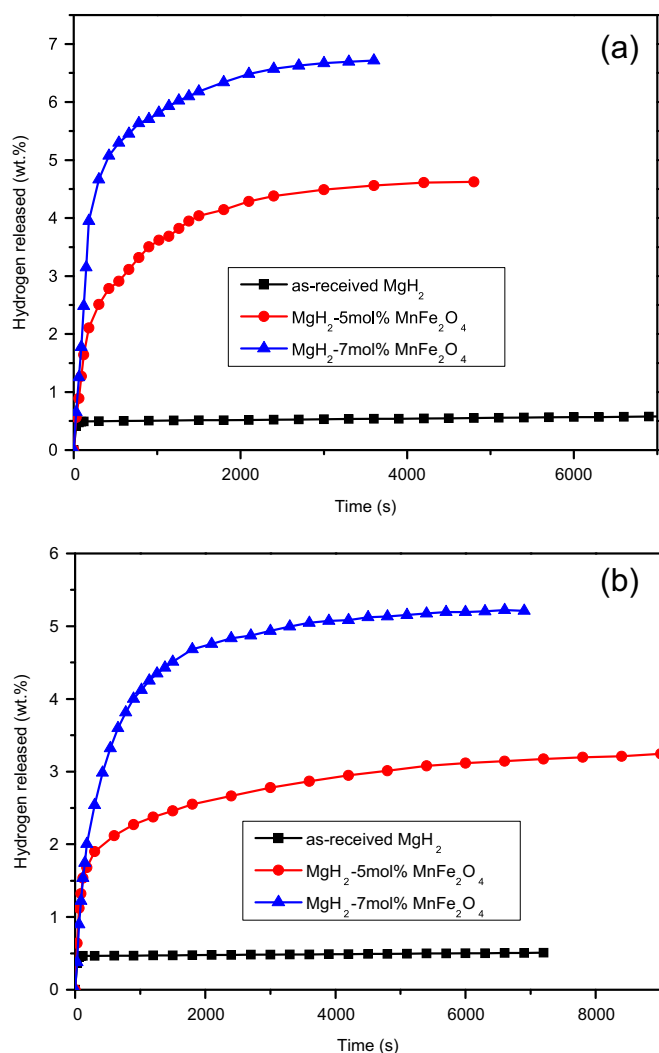


Fig. 3. Isothermal desorption curves of the as-received MgH₂ and ball-milled MgH₂ doped with 5 mol% and 7 mol% MnFe₂O₄ at (a) 350 °C and (b) 300 °C under 0.1 MPa pressure.

reduction in the onset desorption temperature by 110 °C and 120 °C, respectively. Further 7 mol% MnFe₂O₄ addition drops the decomposition initiation temperature to 300 °C, resulting in further decrease, compared with 3 mol% and 5 mol% doped samples, and a reduction of 140 °C, compared with the as-received MgH₂. With the MnFe₂O₄ amount increasing to 9 mol%, the onset dehydrogenation temperature reduces to 280 °C. The reduction of the onset dehydrogenation temperature is 31.8% after doping with MnFe₂O₄

nanopowders, which demonstrates MnFe₂O₄ superiority in improving the MgH₂ desorption temperature, compared with other various catalysts reported in the literature [22–24]. However, hydrogen desorption capacity for the 9 mol% doped sample is significantly lower due to an excess amount of MnFe₂O₄ nanoparticles. Therefore, the MgH₂ + 7 mol% MnFe₂O₄ sample exhibits optimal dehydrogenation performance, including the onset dehydrogenation temperature and the released hydrogen capacity. Thus, using the optimal 7 mol% amount of MnFe₂O₄ nanoparticles, allows analyzing the MnFe₂O₄ mechanism and the catalytic effect in the following test.

To further compare the thermal decomposition performance of MgH₂, with and without the catalyst, Fig. 2 shows DSC curves of the as-received MgH₂ and MgH₂ doped with 7 mol% MnFe₂O₄ samples within the 50–500 °C temperature range (4 °C min^{−1} heating rate). As seen in Fig. 2(a), the DSC curve of the as-received MgH₂ includes only one endothermic peak at 411.2 °C, corresponding to MgH₂ dehydrogenation. However, for the doped sample, there are two characteristic peaks in the DSC curve seen in Fig. 2(b). The first endothermic peak is assigned to MgH₂ desorption, while the origin of the second endothermic peak appearance is unclear. The second peak may be related to the particle size of MgH₂ and the appearance of the γ-MgH₂ phase (Fig. 5(b)) [22,25–27].

The notable reduction of the peak temperature in the above DSC results reveals that the dehydrogenation properties of MgH₂ are significantly improved by adding nanosized MnFe₂O₄. However, it is noteworthy that the desorption temperature onset measured by DSC is quite lower than that measured by PCT. A similar phenomenon is reported in the literature [28,29]. This is mainly due to the different decomposition atmospheres and heating rates for the samples tested with DSC (0.1 MPa argon, 4 °C min^{−1}) and PCT (0.1 atm, 6 °C min^{−1}), resulting in different driving forces during the desorption process.

3.2. Dehydrogenation kinetics

Isothermal desorption kinetics curves for the as-received MgH₂, MgH₂ + 5 mol% MnFe₂O₄ and MgH₂ + 7 mol% MnFe₂O₄ samples are measured at 300 °C and 350 °C respectively under 0.1 MPa pressure. Fig. 3 shows that the as-received MgH₂ and the ball-milled samples doped with 5 mol% MnFe₂O₄ and 7 mol% MnFe₂O₄ nanoparticles release 0.49 wt.%, 2.87 wt.% and 5.05 wt.% hydrogen at 300 °C in 1 h under 0.1 MPa pressure, respectively. Further temperature increase to 350 °C results in 0.54 wt.%, 4.56 wt.% and 6.72 wt.% of released H₂ for the same time and pressure, which demonstrates MnFe₂O₄ superiority in improving MgH₂ desorption kinetics, compared with other catalysts reported in the literature [16,30–33]. Therefore, significant improvement of MgH₂ dehydrogenation kinetics can be achieved by adding MnFe₂O₄ nanopowders.

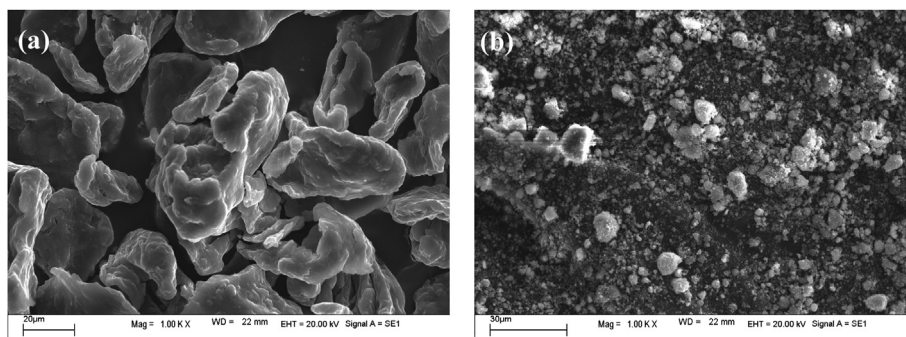


Fig. 4. SEM images of (a) the as-received MgH₂ and (b) ball-milled MgH₂ doped with 7 mol% MnFe₂O₄.

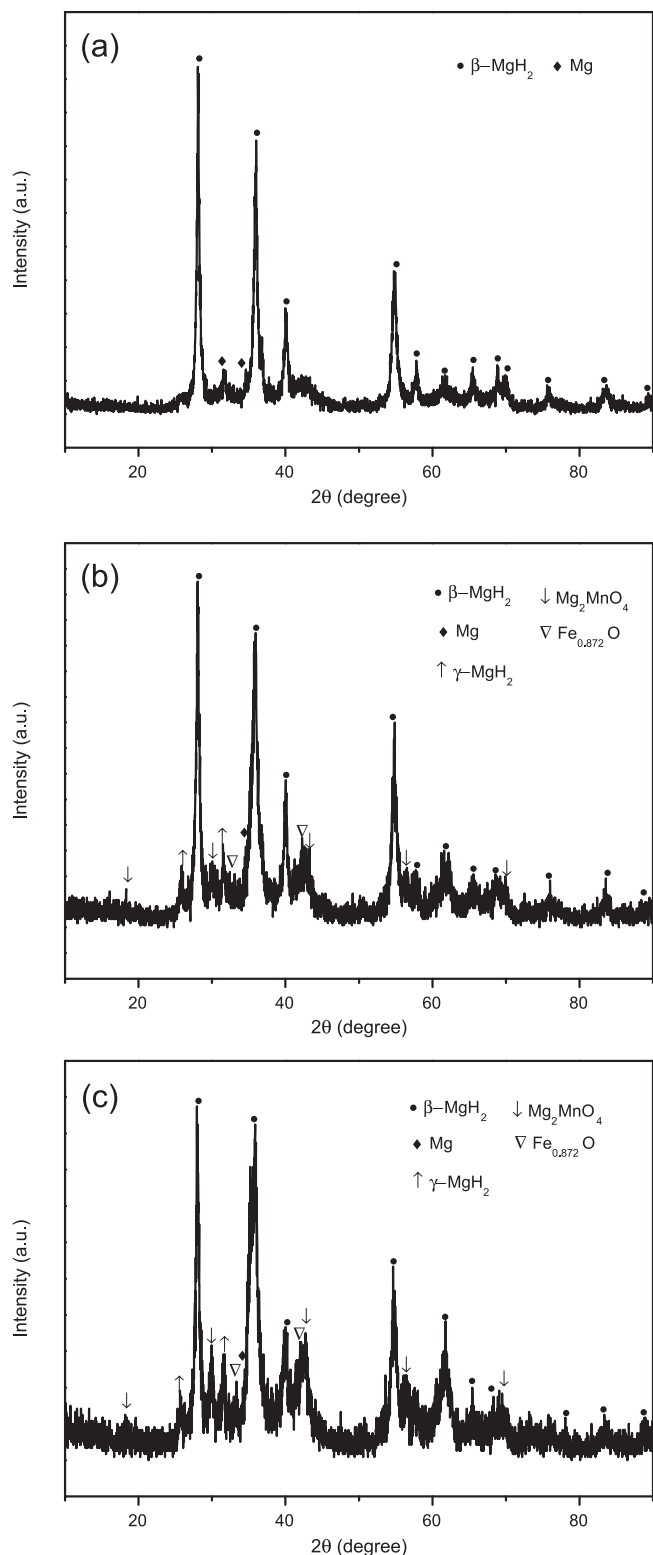


Fig. 5. XRD patterns of (a) as-milled, (b) ball-milled MgH_2 , doped with 3 mol% and (c) 7 mol% MnFe_2O_4 .

3.3. Dehydrogenation mechanism

SEM images of the as-received MgH_2 and the ball-milled MgH_2 sample doped with 7 mol% MnFe_2O_4 nanopowders are shown in Fig. 4. The particle size of the as-received MgH_2 is larger than

100 μm , however, the particle size of the MnFe_2O_4 -doped sample is between 5 μm and 10 μm . It must be mentioned that the embedded MnFe_2O_4 particles can not be seen at the MgH_2 surface by SEM because of their small size. The dehydrogenation properties of MgH_2 doped with MnFe_2O_4 significantly improve after ball milling due to the decreased particle size, which results in high surface defect density and more grain boundaries. Moreover, a high density of nanosized catalyst particles forms a large number of nucleation sites at the surface of the MgH_2 matrix, leading to surface activation and larger surface area of the MgH_2 particles.

In order to further analyze MgH_2 desorption mechanism after doping with MnFe_2O_4 , an apparent activation energy (E_a) of the as-received MgH_2 and MgH_2 doped with 7 mol% MnFe_2O_4 was obtained by the Kissinger method. The E_a of the as-received MgH_2 is 254.89 kJ mol^{-1} , while the E_a of the doped sample is calculated to be 64.55 kJ mol^{-1} . Therefore, there is a remarkable reduction of 190.44 kJ mol^{-1} in E_a for MgH_2 , indicating that the apparent activation energy is significantly improved by adding MnFe_2O_4 nanoparticles. To show MnFe_2O_4 catalytic effect on MgH_2 dehydrogenation, comparison of E_a for MgH_2 doped with different transition metal oxide catalysts, calculated by the Kissinger method, is listed in Table 1 [16,27,34,35]. MnFe_2O_4 -doped sample has the lowest apparent activation energy, which signifies MnFe_2O_4 superiority in improving the desorption performance of MgH_2 , compared with other reported catalysts.

To illustrate that MgH_2 and MnFe_2O_4 react during ball milling, Fig. 5 shows XRD patterns of the as-received MgH_2 (Fig. 5(a)) and MgH_2 doped with 3 mol% (Fig. 5(b)) and 7 mol% (Fig. 5(c)) MnFe_2O_4 after ball milling. Diffraction peaks of the composites are considerably broadened as a consequence of particle size reduction (also confirmed by SEM), more defects and mechanical strains created within the lattice by the ball milling. For the doped samples after ball milling, γ - MgH_2 diffraction reflections appear, but not β - MgH_2 . The presence of γ - MgH_2 is a result of microstructure alteration due to the ball milling, which is in agreement with reported results [36–38]. New Mg_2MnO_4 and $\text{Fe}_{0.872}\text{O}$ phases are found, indicating that MgH_2 and MnFe_2O_4 react during ball milling. A similar decomposition reaction occurs between MgH_2 and Nb_2O_5 , in which Nb_2O_5 reduction forms $\text{MgNb}_2\text{O}_{3.67}$ [39]. Further increase of the MnFe_2O_4 amount results in Mg_2MnO_4 and $\text{Fe}_{0.872}\text{O}$ peaks intensity gradual increase. However, MgH_2 peaks intensity declines, suggesting that MgH_2 reacts with MnFe_2O_4 and experiences partial decomposition during ball milling, which becomes more severe with increasing MnFe_2O_4 amount.

In order to determine the phase structure of the doped samples in desorption process, XRD scans are performed on the as-milled MgH_2 (Fig. 6(a)) as well as 3 mol% (Fig. 6(b)) and 7 mol% (Fig. 6(c)) MnFe_2O_4 -doped samples after desorption at 350 $^\circ\text{C}$, as shown in Fig. 6. For the as-milled MgH_2 , the XRD pattern shows that the sample only has Mg phase after desorption. For the doped samples, the XRD spectra imply that there is not only Mg phase, but

Table 1

Activation energy of MgH_2 doped with different catalysts, calculated by the Kissinger method.

Catalyst	E_a (kJ mol^{-1})		Reference
	Before doping	After doping	
BaRuO ₃	140	90	[16]
VO ₂ (B)	160	139	[27]
Cr ₂ O ₃	—	84	[34]
TiO ₂	—	94	[34]
Fe ₂ O ₃	—	124	[34]
Fe ₃ O ₄	—	115	[34]
Nb ₂ O ₅	206	197	[35]
MnFe_2O_4	254.89	64.55	This work

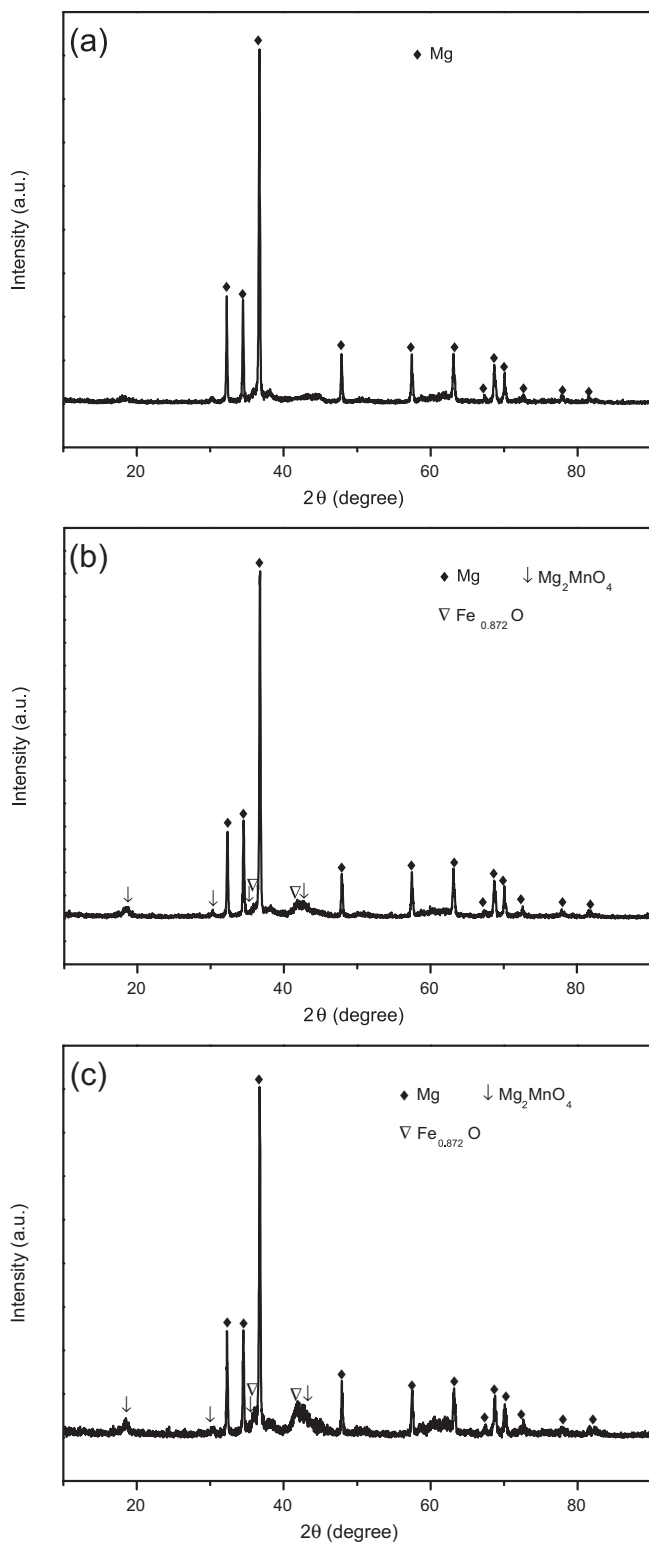


Fig. 6. XRD patterns of (a) as-milled, (b) ball-milled MgH_2 , doped with 3 mol% and (c) 7 mol% MnFe_2O_4 after desorption.

also Mg_2MnO_4 and $\text{Fe}_{0.872}\text{O}$ phases. The $\text{Fe}_{0.872}\text{O}$ phase reflections intensity gradually increases with the amount of MnFe_2O_4 . Considering the extreme improvement of MgH_2 desorption properties by doping with MnFe_2O_4 , it is reasonable to conclude that the formed Mg_2MnO_4 and $\text{Fe}_{0.872}\text{O}$ phases together provide a synergistic catalytic effect.

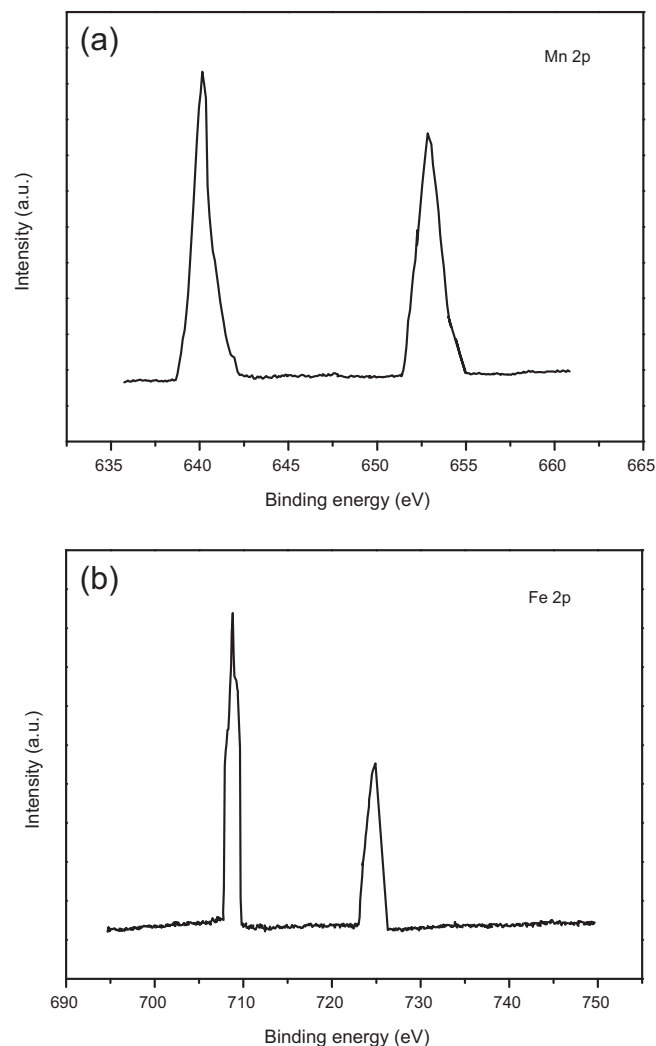


Fig. 7. Narrow scan XPS spectra of MgH_2 doped with 7 mol% MnFe_2O_4 after ball milling (a) Mn 2p and (b) Fe 2p.

Fig. 7 shows the XPS narrow scan spectra of the ball-milled MgH_2 doped with 7 mol% MnFe_2O_4 . **Fig. 7(a)** shows the photoemission spectrum of Mn 2p at 640.2 eV and 652.9 eV, corresponding to Mg_2MnO_4 and MnO_x/Mn , respectively. **Fig. 7(b)** shows the photoemission spectrum of Fe 2p at 707 eV and 725 eV, respectively, corresponding to Fe_xO_y and Mg_2MnO_4 . XPS results further testify that MgH_2 and MnFe_2O_4 react during ball milling.

4. Conclusions

In conclusion, the dehydrogenation properties of MgH_2 are remarkably improved by adding MnFe_2O_4 nanoparticles. The onset desorption temperature of ball-milled MgH_2 doped with 7 mol% MnFe_2O_4 is 300 °C, resulting in 140 °C decrease, compared with the as-received MgH_2 . The isothermal dehydriding kinetics shows that 7 mol% MnFe_2O_4 -doped sample can release 5.05 wt.% hydrogen in 1 h under 0.1 MPa pressure, whereas as-received MgH_2 only releases 0.54 wt.% hydrogen for the same conditions (time, temperature and pressure). From the differential scanning calorimetry and the Kissinger desorption kinetics analyses, the apparent activation energy E_a of the 7 mol% MnFe_2O_4 -doped sample is 64.55 kJ mol⁻¹, resulting in 190.34 kJ mol⁻¹ reduction, compared with the as-received MgH_2 sample. Based on X-ray diffraction and X-ray

photoelectron spectroscopy analyses, Mg_2MnO_4 and $\text{Fe}_{0.872}\text{O}$ phases together play a synergistic role in remarkably improving dehydrogenation properties of MgH_2 .

Acknowledgments

The authors acknowledge the financial support from the National High-Tech R&D Program (863 Program) of China (2006AA05Z132) and China Scholarship Council. AV acknowledges support from the National Science Foundation.

References

- [1] I.P. Jain, Int. J. Hydrogen Energy 34 (2009) 7368–7378.
- [2] I.P. Jain, C. Lal, A. Jain, Int. J. Hydrogen Energy 35 (2010) 5133–5144.
- [3] M.Y. Song, Y.J. Kwak, S.H. Lee, J. Song, D.R. Mumm, Int. J. Hydrogen Energy 37 (2012) 18133–18139.
- [4] H. Gasan, O.N. Celik, N. Aydinbeyli, Y.M. Yaman, Int. J. Hydrogen Energy 37 (2012) 1912–1918.
- [5] S.A. Pighina, G. Capurso, S. Lo Russo, J. Alloys Compd. 530 (2012) 111–115.
- [6] B. Paik, I.P. Jones, A. Walton, V. Mann, D. Book, I.R. Harris, J. Alloys Compd. 492 (2010) 515–520.
- [7] M. Tanniru, D.K. Slattery, F. Ebrahimi, Int. J. Hydrogen Energy 35 (2010) 3555–3564.
- [8] L. Xie, Y. Liu, X. Zhang, J. Qu, Y. Wang, X. Li, J. Alloys Compd. 248 (2009) 388–392.
- [9] M. Polanski, J. Bystrzycki, R.A. Varinb, T. Plocinski, M. Pisarek, J. Alloys Compd. 509 (2011) 2386–2391.
- [10] L.-P. Ma, P. Wang, H.-M. Cheng, Int. J. Hydrogen Energy 35 (2010) 3046–3650.
- [11] M.O.T. da Conceição, M.C. Brum, C.S. Guimarães, D.S. dos Santos, J. Alloys Compd. 536 (2012) S255–S258.
- [12] M.O.T. da Conceição, M.C. Brum, D.S. dos Santos, M.L. Dias, J. Alloys Compd. 550 (2013) 179–184.
- [13] T.K. Nielsen, T.R. Jensen, Int. J. Hydrogen Energy 37 (2012) 13409–13416.
- [14] M.W. Rahman, S. Livraghi, F. Dolci, M. Baricco, E. Giamello, Int. J. Hydrogen Energy 36 (2011) 7932–7936.
- [15] M.W. Rahman, A. Castellero, S. Enzo, S. Livraghi, E. Giamello, M. Baricco, J. Alloys Compd. 509S (2011) S438–S443.
- [16] M. Baricco, M.W. Rahman, S. Livraghi, A. Castellero, S. Enzo, E. Giamello, J. Alloys Compd. 536 (2011) S216–S221.
- [17] Z.W. Cong, S. Fei, Trans. Nonferrous Met. Soc. China 19 (2009) 606–610.
- [18] M.Y. Song, S.N. Kwon, D.R. Mumm, S.-H. Hong, Curr. Appl. Phys. 9 (2009) S118–S120.
- [19] F. Zhai, P. Li, A. Sun, S. Wu, Q. Wan, W. Zhang, Y. Li, L. Cui, X. Qu, J. Phys. Chem. C 116 (2012) 11939–11945.
- [20] Y. Jia, Y. Guo, J. Zou, X. Yao, Int. J. Hydrogen Energy 37 (2012) 7579–7585.
- [21] A. Zaluska, L. Zaluski, J.O. Strom-Olsen, J. Alloys Compd. 288 (1999) 217–225.
- [22] M. Cabo, S. Garroni, E. Pellicer, C. Milanese, A. Girella, A. Marini, E. Rossinyol, S. Suriñach, M.D. Baró, Int. J. Hydrogen Energy 36 (2011) 5400–5410.
- [23] J. Mao, Z. Guo, X. Yu, H. Liu, Z. Wu, J. Ni, Int. J. Hydrogen Energy 35 (2010) 4569–4575.
- [24] A. Ranjbar, Z.P. Guo, X.B. Yu, D. Wexler, A. Calka, C.J. Kimd, H.K. Liu, Mater. Chem. Phys. 114 (2009) 168–172.
- [25] J. Huot, G. Liang, S. Boily, A. Van Neste, R. Schulz, J. Alloys Compd. 293–295 (1999) 495–500.
- [26] R.A. Varin, T. Czujko, Z. Wronski, Nanotechnology 17 (2006) 3856–3865.
- [27] S. Milosevic, Z. Raskovic-Lovre, S. Kurko, R. Vujasin, N. Cvjetanin, L. Matovic, J. Grbovic-Novakovic, Ceram. Int. 39 (2013) 51–56.
- [28] H. Imamura, K. Tanaka, I. Kitazawa, T. Sumi, Y. Sakata, N. Nakayama, S. Ooshima, J. Alloys Compd. 484 (2009) 939–942.
- [29] M.-Q. Fan, S.-S. Liu, Y. Zhang, J. Zhang, L.-X. Sun, F. Xu, Energy 35 (2010) 3417–3421.
- [30] M.Y. Song, Y.J. Kwak, H.R. Park, S.-H. Hong, J. Ind. Eng. Chem. 17 (2011) 700–704.
- [31] F. Tonus, V. Fuster, G. Urretavizcaya, F.J. Castro, J.-L. Bobet, Int. J. Hydrogen Energy 34 (2009) 3404–3409.
- [32] M.Y. Song, S.N. Kwon, H.R. Park, D.R. Mumm, J. Ind. Eng. Chem. 17 (2011) 167–169.
- [33] M.Y. Song, Y.J. Kwak, B.-S. Lee, H.R. Park, B.-G. Kim, Int. J. Hydrogen Energy 37 (2012) 1531–1537.
- [34] M. Polanski, J. Bystrzycki, J. Alloys Compd. 486 (2009) 697–701.
- [35] A. Patah, A. Takasaki, J.S. Szmyd, Int. J. Hydrogen Energy 34 (2009) 3032–3037.
- [36] A. Ranjbar, M. Ismail, Z.P. Guo, X.B. Yu, H.K. Liu, Int. J. Hydrogen Energy 35 (2010) 7821–7826.
- [37] A. Ranjbar, Z.P. Guo, X.B. Yu, D. Attard, A. Calka, H.K. Liu, Int. J. Hydrogen Energy 34 (2009) 7263–7268.
- [38] N. Mahmoudi, A. Kaflou, A. Simchi, J. Power Sources 196 (2011) 4604–4608.
- [39] O. Friedrichs, J.C. Sanchez-López, C. López-Cartes, T. Klassen, R. Bormann, A. Fernandez, J. Phys. Chem. B 110 (2006) 7845–7850.